AIAA JOURNAL
Vol. 44, No. 9, September 2006

Experimental Investigation of Reynolds and Favre Averaging in High-Speed Jets

J. Panda*
Ohio Aerospace Institute, Brookpark, Ohio 44135
and
R. G. Seasholtz†
NASA John H. Glenn Research Center at Lewis Field, Brookpark, Ohio 44135

Recent advancements in a molecular Rayleigh scattering based diagnostic technique allowed for simultaneous measurement of velocity and density fluctuations with high sampling rates. The technique was used to investigate unheated high subsonic and supersonic fully expanded free jets in the Mach number range from 0.8 to 1.8. The difference between the Favre-averaged and the Reynolds-averaged axial velocity and axial component of the turbulent kinetic energy is found to be small. On average, estimates based on Morkovin's strong Reynolds analogy are found to underpredict turbulent density fluctuations.

I. Introduction

NUMERICAL modeling of many aerospace applications requires information on the changes of turbulence statistics with an increase of the flow Mach number. To account for this compressibility effect, modeling efforts use various assumptions that need to be validated experimentally. The primary difficulty in the validation efforts lies with the limitations of existing experimental tools, such as hot-wire anemometers, to provide turbulence statistics in realistic Mach number and Reynolds number flows. In some instances, insights obtained from measurements of low-speed flows are perhaps applicable to higher Mach number conditions; however, the progressive deviations need to be estimated. In other instances, where scalar fluctuations (density, temperature, and pressure fluctuations) and their transport by the velocity fluctuations are involved, modeling requires new sets of statistical parameters that are absent in the incompressible counterpart. One such example is the use of Favre-averaged parameters in compressible turbulence modeling. Reynolds averaging, used in the incompressible counterpart, involves dividing a fluid flow parameter w into a time-averaged $\bar{w}$, and a fluctuating w' part,

$$w(t) = \bar{w} + w'(t), \qquad \bar{w} = \lim_{T\to\infty} \frac{1}{T}\int_0^T w\,\mathrm{d}t \tag{1}$$

In Favre averaging[1] (see Ref. 2) a density-weighted filter is used to calculate the time average $\tilde{w}$ and the remaining fluctuating part w'',

$$w(t) = \tilde{w} + w''(t), \qquad \tilde{w} = \frac{1}{\bar{\rho}} \lim_{T\to\infty} \frac{1}{T}\int_0^T \rho w\,\mathrm{d}t \tag{2}$$

where ρ denotes air density. Because there is no mass flux across a Favre-averaged streamline, the use of Favre-averaged variables makes the governing equations for mean density, mean velocity, and mean enthalpy more compact. In compressible flow, such simplifications are unattainable by the Reynolds-averaging process. Experimental data, such as those measured by particle image velocimetry and the present Rayleigh scattering technique, however, produce Reynolds-averaged quantities. The differences between the two averages for parameters such as the axial velocity u and the turbulent kinetic energy become a concern whenever computational results are to be compared to experimental data. The first goal of the present experimental effort is to determine the differences experimentally by measuring correlations between density and axial velocity fluctuations. In the past, Bowersox[3] used laser Doppler anemometry in conjunction with hot wires to measure Favre-averaged velocity and Reynolds stresses. However, the experiments were conducted in boundary-layer flows where fluctuation levels are much smaller than that of freejets.

A second goal of the present work is to validate Morkovin's strong Reynolds analogy[4] (SRA) in freejets. The origin of Favre averaging to remove density fluctuations from the time-averaged equations of motion lies with this hypothesis. The original Reynolds analogy shows that in bounded shear layers the heat transfer coefficient from the wall is related to the skin-friction coefficient.[5] Physically, it states that turbulence-induced heat and momentum transfer normal to the wall happen in the same manner. Morkovin's derivation of the SRA extended this connection to compressible flows.[4] As a special case of negligible total temperature T_0 and static pressure p fluctuations, he showed that the turbulent density ρ and temperature T fluctuations are simply related to the velocity fluctuations via the following:

$$p'/p \ll 1, \qquad T_0'/T_0 \ll 1$$

so that

$$\rho'/\bar{\rho} \approx -T'/\bar{T} \approx (\gamma - 1)M^2(u'/\bar{u}) \tag{3}$$

All variables in Eq. (3) indicate local values, with primes indicating fluctuating quantities and overbars indicating time-averaged quantities. Additionally, γ is the ratio of specific heats, u is the axial component of velocity, and M is the local Mach number based on the local velocity and the local speed of sound. Bradshaw[6] estimated that Eq. (3) remains valid in boundary layers and wakes for freestream Mach number less than five and in freejets for Mach number less than 1.5.

Validation of Morkovin's hypothesis and measurement of the Favre-averaged variables have been attempted in the past using hot-wire anemometry. The analysis of hot-wire signals becomes involved and carries various assumptions for applications in compressible flows. In free shear layers, hot wires break easily, and simultaneous velocity and temperature/density measurements become difficult. Nevertheless, Gaviglio[7] showed that the SRA is reasonably satisfied in boundary-layer flow in the absence of significant heat transfer across the wall. Barre et al.[8] measured velocity and temperature fluctuations in a supersonic mixing layer and validated

Presented as Paper 2005-0514 at the AIAA Aerospace Sciences Meeting, Reno, NV, 10–13 January 2005; received 19 January 2005; revision received 23 December 2005; accepted for publication 23 December 2005.

*Senior Scientist; currently with Acoustic Branch, NASA John H. Glenn Research Center at Lewis Field, Brookpark, OH 44135. Associate Fellow AIAA.
†Optical Instrumentation and NDE Branch; retired.

Morkovin's hypothesis. The authors do not know of any earlier study to validate the SRA in freejets. The turbulence structure of freejets, especially downstream of the potential core where a lip shear layer merges, is different from that found in wall-bounded flows or in simple mixing layers. A special requirement of the SRA is negligible total temperature fluctuations. The unheated jets used for the present tests have the same plenum temperature as that of the ambient. Because the total temperature was constant everywhere in the flowfield, Morkovin's conditions were well satisfied. Therefore, the unheated jets presented a good opportunity to validate the SRA in freejets.

The present measurements have been made possible due to the advances[9,10] in a molecular Rayleigh scattering based technique to measure density and velocity fluctuations in high-speed flows simultaneously. Fluctuations occurring over a frequency range of 0–45 kHz have been measured. The technique is based on laser light scattering from the gas molecules that make up air. Because neither seed particles nor intrusive probes are used, the technique is strictly noninvasive. Implementation of the technique requires special attention to the cleanliness of the airstream, isolation of the sensitive optical components from jet noise, usage of a Fabry–Perot interferometer, and low-level light measuring electronics. A description of the technique is provided later in the text.

The present work is part of a database development project, and the freejets used for the current investigation were also the subject of some of the earlier studies. The time-averaged velocity, temperature, and density surveys from these jets have been reported earlier.[11] Schlieren photographs and various statistics of density fluctuations were provided by Panda and Seasholtz.[12] The far-field noise sources were identified by correlating turbulent density and velocity fluctuations with far-field noise pressure fluctuations.[12,13]

A. Difference Between Favre-Averaged and Reynolds-Averaged Axial Velocity and Axial Component of Kinetic Energy

Following the definitions of Reynolds averaging and Favre averaging shown in Eqs. (1) and (2),

$$\tilde{u} = \overline{\rho u}/\bar{\rho} = \overline{(\rho' + \bar{\rho})(u' + \bar{u})}/\bar{\rho} = \bar{u} + \overline{\rho' u'}/\bar{\rho} \tag{4}$$

Hence,

$$\tilde{u} - \bar{u} = \overline{\rho' u'}/\bar{\rho} \tag{5}$$

Therefore, the difference in the time-averaged velocity is due to the correlations between the density and velocity fluctuations. A similar equation holds for the fluctuating terms. Because $\tilde{u} + u'' = \bar{u} + u'$,

$$u' - u'' = \overline{\rho' u'}/\bar{\rho} \tag{6}$$

Next, the kinetic energy is considered, which involves products of fluctuations. For example, Reynolds-averaged kinetic energy is $k = 0.5(\overline{u'u'} + \overline{v'v'} + \overline{w'w'})$, where v and w represent, respectively, the radial and tangential components of velocity. In the present program, only the axial component of velocity was measured. The axial component of kinetic energy in Favre-averaged functuations is

$$\widetilde{u''u''} = \overline{\rho u'' u''}/\bar{\rho} = \overline{(\bar{\rho} + \rho')u'' u''}/\bar{\rho} = \overline{u'' u''} + \overline{\rho' u'' u''}/\bar{\rho} \tag{7}$$

When Eq. (6) is used, the first term on the right-hand side can be expressed as

$$\overline{u'' u''} = \overline{u' u'} + (\overline{\rho' u'}/\bar{\rho})^2 \tag{8}$$

The second term on the right-hand side of Eq. (7) can also be written as

$$\overline{\rho' u'' u''}/\bar{\rho} = \overline{\rho' u' u'}/\bar{\rho} - 2(\overline{\rho' u'}/\bar{\rho})^2 \tag{9}$$

Hence, the difference in axial component of kinetic energy is

$$\tfrac{1}{2}(\widetilde{u''u''} - \overline{u'u'}) = \tfrac{1}{2}\{(\overline{\rho' u' u'})/\bar{\rho} - (\overline{\rho' u'}/\bar{\rho})^2\} \tag{10}$$

This equation shows that, in addition to density–velocity correlations, density–velocity squared correlations have significant contributions to the difference. In the present work, these two correlations were calculated from cross correlations defined as

$$\langle \rho'; u' \rangle(\tau) = \frac{1}{T}\int_0^T \rho'(t) u'(t+\tau)\,\mathrm{d}t$$

$$\langle \rho'; u'u' \rangle(\tau) = \frac{1}{T}\int_0^T \rho'(t)[u'(t+\tau)]^2\,\mathrm{d}t \tag{11}$$

where τ is the correlation time or delay time and T is the duration of the measured data. Note that by definition

$$\overline{\rho' u'} = \langle \rho'; u' \rangle_{\tau=0}, \qquad \overline{\rho' u' u'} = \langle \rho'; u'u' \rangle_{\tau=0} \tag{12}$$

B. Fundamentals of Flow Measurement Using Molecular Rayleigh Scattering

A simplistic description of the measurement process using laser-induced Rayleigh scattering is schematically shown in Fig. 1. When a laser beam is allowed to pass through a gas, the molecules present in the gas cause light scattering. The Rayleigh scattering process describes most (~99%) of the molecular scattered light. In the present experiment, scattered light is collected and spectrally resolved to measure velocity. The line width of the incident laser beam is very narrow, whereas that of the Rayleigh scattered light is broad. Even if the gas medium is stationary, the random thermal motion of the gas molecules creates a wide range of Doppler shift, resulting in spectral broadening of the collected light. The full width at half-maximum of the spectrum is a function of the distribution of molecular velocities and, therefore, is a measure of gas temperature. In the case of a moving gas media, the bulk velocity is superimposed on the random thermal motion of the individual molecules; therefore, the separation between the peaks of the incident laser line and the Rayleigh spectrum provides a measure of the bulk velocity. The total light under the Rayleigh spectrum is proportional to the molecular number density and provides a measure of gas density. Thus, a single Rayleigh spectrum carries information of one component of gas bulk velocity, temperature, and density.

This basic principle has been used in the past to measure time-averaged quantities. Because density variation modulates the total scattered light, unsteady density fluctuations are relatively easy to measure. Extension of the Rayleigh scattering technique to measure unsteady velocity fluctuations has remained a challenge. Recently, Seasholtz et al.[9,10] have simultaneously measured the time variation of density and velocity fluctuations in freejets. The present setup is for a point-measurement system; a single-frequency, continuous-wave laser was used, and scattered light from a small region was spectrally analyzed using a Fabry–Perot interferometer.

To illustrate the unsteady velocity measurement process, first the nature of a fringe formed by the interferometer is shown in Fig. 2. The interferometer and associated optics basically image the fiber end delivering the scattered light. Because the fiber diameter is small, the field of view in the image covers a fraction of the free spectral range. The spectral analysis is a two-step process. First, a small portion of the light taken directly from the laser beam is

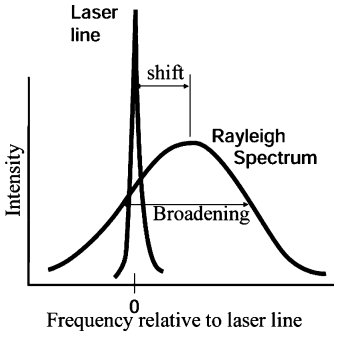

Fig. 1 Schematic of Rayleigh spectrum from airflow.

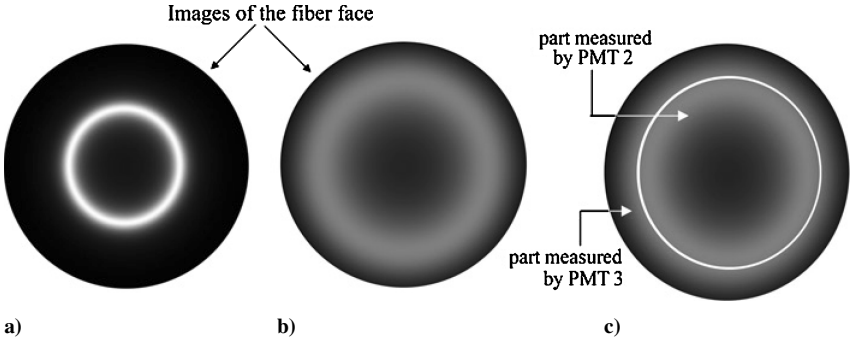

Fig. 2 Fringes formed after passing through Fabry–Perot interferometer by a) incident laser light b) Rayleigh scattered light, and c) splitting of Rayleigh image to measure velocity fluctuations.

imaged through the interferometer. (The Rayleigh scattered light is blocked; instead a part of the unscattered incident laser beam is analyzed.) The narrow line width of the laser makes a sharp, narrow ring in this image (reference image; Fig. 2a). In the second step, the Rayleigh scattered light from a moving gas medium is passed through the fiber. The image formed by the Fabry–Perot interferometer (Rayleigh image; Fig. 2b) is different: A diffused ring with a different ring diameter results. The radial shift in the peak intensity locations between the Rayleigh and the reference images is related to the Doppler shift associated with the bulk motion of the airstream. (The diffused nature of the Rayleigh image is due to the thermal broadening.) Because the laser frequency and, therefore, the reference fringe are fixed, an instantaneous change of air velocity produces a radial shift of the ring seen in the Rayleigh image. To measure the time variation of velocity, one needs to monitor the ring diameter in the Rayleigh image. To this end, Seasholtz et al.[9] used an image dissector that split the Rayleigh image into two concentric parts (Fig. 2c), and measured the ratio of light intensities from the inner and the outer parts using two photomultiplier tubes (PMT). The ratio of photoelectron counts from the two PMTs carried information about the ring diameter variation in the Rayleigh image, which in turn reflected the change of Doppler shift frequency from the velocity change at the probe volume. For calibration, the intensity variations from the two parts were measured from known velocity flows. It was found that the intensity variation with velocity in both parts of the image can be modeled by second-order polynomials. If N_2 and N_3 denote photoelectron count rates from the inner and outer PMTs, then,

$$N_2 = A_i + uB_i + u^2C_i, \qquad N_3 = A_o + uB_o + u^2C_o \tag{13}$$

Where A_i, B_i, C_i, A_o, B_o, and C_o are calibration constants. The velocity component u is measured from a ratio of the two counts, $R = N_3/N_2$,

$$u = \left[-(RB_i - B_o) + \sqrt{(RB_i - B_o)^2 - 4(RA_i - A_o)(RC_i - C_o)}\right] \Big/ [2(RC_i - C_o)] \tag{14}$$

Note that the ratio of the two counts cancels out changes in the overall scattering intensity associated with flow density variation. Also, the physically meaningful, positive root of the quadratic equation is considered. The component of velocity measured using a given optical arrangement depends on the angular position of the collection lens with respect to the incident laser beam. The present setup, shown in Fig. 3, measured the axial velocity component. Note that the setup measures negative u velocity. The calibration process accounted for the sign reversal. The Rayleigh scattered light was collected and transmitted to an adjoining room for spectral analysis. Figure 4 shows a schematic of the spectroscopic arrangement.

An important caveat in the preceding analysis is an implicit assumption that the effect of temperature fluctuations is also accounted for via the calibration process. Temperature broadening results in changes of light intensity in both the inner and outer parts of the image. By virtue of measuring a ratio of intensities between the two parts of the image, the process was made somewhat insensitive to temperature fluctuations. A numerical uncertainty analysis[10]

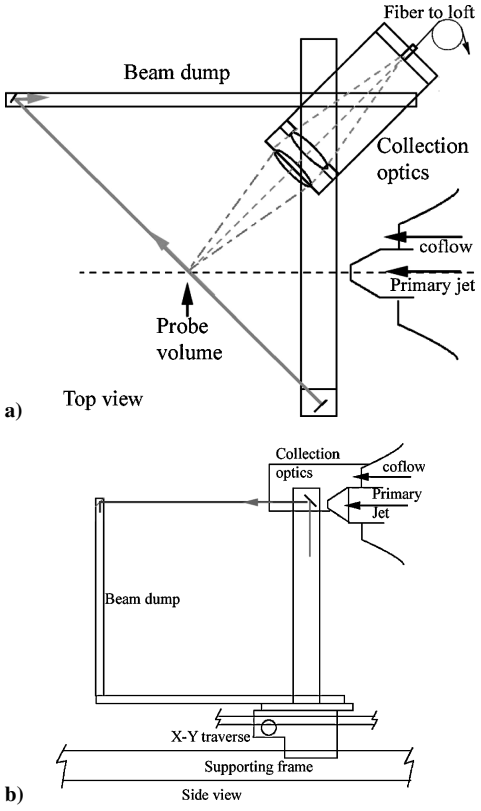

Fig. 3 Optical arrangement to measure axial u component of velocity: a) top view and b) side view.

demonstrates that the effect of temperature fluctuation is small compared to the bigger change associated with velocity fluctuations. In addition, the present experiment was conducted in the potential core of the same freejets used to obtain the calibration constants. Hence, the influence of isentropic temperature fluctuations was automatically included in the calibration constant. However, nonisentropic temperature fluctuations have affected the velocity fluctuations data in a small yet unknown way.

To measure density fluctuations, about 10% of the Rayleigh scattered light was split off using a beam splitter (BS1 in Fig. 4), and the intensity fluctuations were monitored using a separate PMT. For a fixed optical setup and a fixed gas composition, the intensity variation of Rayleigh scattered light is directly proportional to air density variation. Once again, a calibration is necessary to relate photoelectron count to density change. The calibration was performed in the same core regions of the jet flows used for velocity calibration. If the local air density is ρ and photoelectron count rate from PMT1 is N_1, then

$$N_1 = C_{\rho 1} + \rho C_{\rho 2} \tag{15}$$

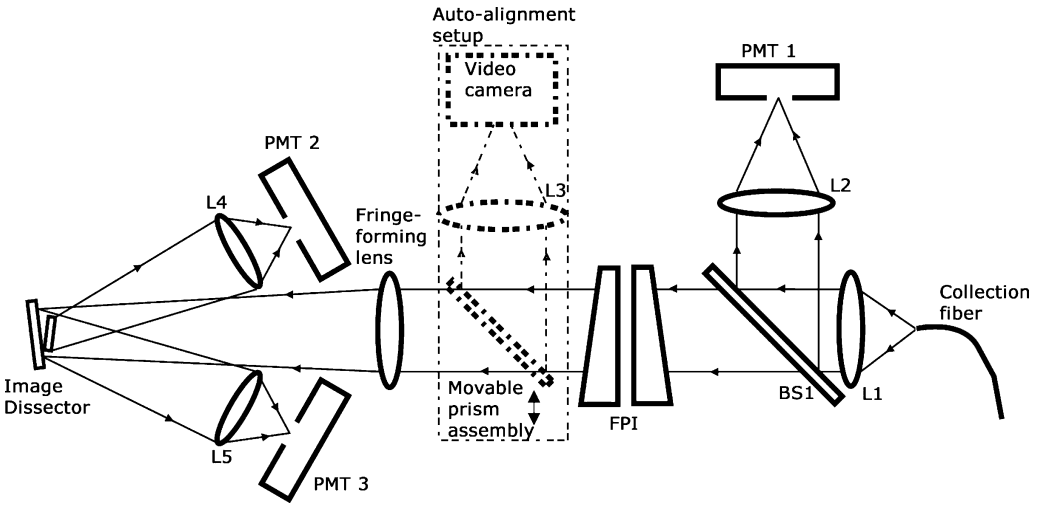

Fig. 4 Schematic of optical setup to analyze collected light: L1–L5, lenses; BS1, beam splitter; and FPI, Fabry–Perot interferometer.

where $C_{\rho 1}$ and $C_{\rho 2}$ are calibration constants. In summary, a total of three PMTs were used: two for measuring velocity and one for density. Additionally, two sets of calibration constants were needed for velocity and density measurements.

II. Experimental Setup

Experiments were performed at NASA John H. Glenn Research Center at Lewis Field using three different nozzles (one convergent and two convergent–divergent) operated at Mach numbers $M = 0.95$, 1.4, and 1.8. The convergent–divergent nozzles were designed by the method of characteristics. All nozzles had a 25.4-mm exit diameter. The jet facility used a continuous supply of unheated compressed air. The Rayleigh scattering system is somewhat elaborate, and the following provides a brief description of some of the central features. An in-depth discussion of the Rayleigh setup can be found in Ref. 13. The optical system was built in two parts. The first part is located in the jet facility and includes the laser, focusing optics, and optics for collecting the scattered light (Fig. 3). The scattered light was then passed through a 0.55-mm-diam optical fiber to a quiet room where the second part of the system, consisting of a spectroscopic system and photon counting electronics, was placed (Fig. 4). The splitting of the setup is necessary to minimize the effect of vibration on the optical components. Additional care had to be taken to reduce dust particles in the airstreams and to stabilize the interferometer from temperature and vibration induced drifts. To reduce dust particles, the dry air, supplied from a central high-pressure facility, was passed through additional micrometer-size filters that made the primary jet air very clean. To clean the entrained ambient air, an additional air blower and filter system was installed that provided a large, 200-mm-diam, low-speed ($\sim$20 m/s) coflow around the 25.4-mm primary jet.

The optical system was mounted on an X–Y traversing unit that carried the laser head, transmission optics, and collection optics. Surveys were made by moving the probe volume from point to point in the plume. The laser head of the solid-state, frequency-doubled Nd:VO_4 laser was placed at the bottom part of the setup. About 5 W of single-frequency, 532-nm wavelength laser light was transmitted through a hollow side beam that contained a half-wave plate, focusing lens, mirrors, and baffles. Because Rayleigh scattered light is polarization-dependent, the half-wave plate was rotated to align the peak scattering plane with the receiving optics. The background scattered laser light was significantly attenuated by suitable use of baffles and a beam dump. It was found that the noise from the jet created a tonal excitement of the laser line at around 430 Hz. To reduce this excitation, an anechoic box was built around the laser head. This box significantly reduced the laser unsteadiness, but a trace remained and was manifested in the experimental results.

To measure the axial component of velocity, the laser beam was passed at 45 deg to the jet axis, and scattered light from 90 deg to the incident direction was collected by lenses placed in the same plane containing the laser beam and the jet axis. The collection optics included a collimator (300-mm focal length, 82-mm-diam achromat) and a focusing lens (160-mm focal length achromat) that imaged the probe volume on the face of a 0.55-mm-diam multimode fiber. The combination of the fiber diameter and the magnification ratio of the collection optics defined the probe volume length as 1.03 mm. Not shown in Fig. 3 is an additional part of the setup where a small part of light from the transmitting laser beam was split off for the purpose of monitoring the laser frequency as well as to maintain the alignment of the Fabry–Perot interferometer. Whenever necessary, a pneumatically actuated mirror was placed in the transmission laser path to divert light toward a diffuser. The mirror also blocked the incident laser beam from going through the jet, and the diffuser scattered the incident light, a small part of which was then collected by the optical fiber.

In the second part of the setup (Fig. 4), light arriving via the optical fiber was collimated by 100-mm focal length lens L1, and about 10% was split from the beam by BS1 and measured by PMT1. Output from PMT1 was proportional to the air density fluctuations. The rest of the collimated beam was passed through a 70-mm aperture planar mirror Fabry–Perot interferometer for spectral analysis. Single-wavelength light from an extended source is imaged as concentric rings (fringes) at the output of the interferometer. However, the restriction of the field of view imposed by the fiber diameter resulted in only one fringe as shown earlier in Fig. 2. The fringe-forming lens, which ultimately images the fiber face on the image dissector, was made of two camera lenses with suitable separation for an effective focal length of 2909 mm. The large magnification ratio of the setup created a 16-mm-diam image of the 0.55-mm-diam fiber on an image dissector. The image dissector was made of two concentric and slightly tilted mirrors. The inner one had a diameter of 10 mm and directed the inner part of the fringe to PMT2, whereas the 25-mm-diam outer one directed the outer part of the fringe to PMT3. The ratio of light intensities from PMT2 and PMT3 provided a measure of either axial or radial velocity as described earlier.

The success of the velocity measurement system was critically dependent on stable operation of the interferometer. Slight thermal drift or change in the incident laser frequency displaced the reference fringe (Fig. 2a), which was manifested as an artificial bias in the velocity measurement. This made the autoalignment setup (Fig. 4) necessary. The alignment system was a feedback control that first measured the reference fringe diameter and compared it with a prescribed targeted diameter. This was accomplished by splitting parts of the transmitted light using a three-prism assembly and imaging them on a charge-coupled device camera. Subsequently, the

difference between the targeted and the measured fringe diameters was translated into a change of high-voltage supply to the piezoelectric actuators that adjusted interferometer's plate separation. Before every Rayleigh measurement, reference light was collected, and the autoalignment system was engaged. When the desired fringe diameter was obtained within a tolerance, the reference light collection system was disengaged, and velocity and density measurement via analysis of the Rayleigh scattered light began.

The avoidance of dust particles is also important for the successful operation of a Rayleigh scattering based system. As mentioned earlier, a clean coflow was created around the primary jet by using a secondary blower and an associated air filtering system. The coflow significantly minimized particle entrainment from the ambient. However, the presence of a few particles is unavoidable. Usually, the passage of a particle is associated with a large increase in the scattered light intensity, which, in turn, manifests as a spike in the time trace of the photoelectron count. Such spikes were rejected during the data processing by substituting counts above four times the standard deviation by the mean count. As expected, the particle count increased as the probe volume was moved farther downstream of the nozzle exit. To avoid excessive contamination, no data were acquired beyond 16 jet diameters. The postprocessing scheme to avoid particle signature could not eliminate weak scattering from particles passing slightly away from the center of the probe volume. The passage of such particles increases the measured mean square fluctuations level. This increase is difficult to quantify and perhaps has added a small level of uncertainty in the measured data.

Photoelectron counting electronics were used with all three PMT signals. The photoelectron pulses from each PMT arriving within a preset gated time interval were counted using a personal computer countertimer board. Counting was performed on contiguous series of gated time intervals without any dead time between the gates. Long time records of up to 5 million data points from each PMT were acquired with a typical sampling rate of 90,000/s. The data points were converted to physical parameters, instantaneous density and velocity, through the usage of proper calibration constants. The Welch method of modified periodograms along with a standard fast Fourier transform routine was used to calculate individual power spectra and cross spectra. Each long record was divided into small, 50% overlapped, segments; modified periodograms of each segment provided local estimates; and the average of all local estimates provided the final power spectra. Time-domain correlation calculations were also performed via Fourier transform, where individual segments of velocity and density time histories were Fourier transformed, multiplied, and inverse transformed. For example, the density–velocity cross correlation was calculated as

$$\langle \rho'; u' \rangle = \Im^{-1}\{\Im[\rho(t)] \times \Im^{*}[u(t)]\} \tag{16}$$

In this equation, $\Im$ represents Fourier transform, complex conjugation is represented by the asterisks, and inverse Fourier transformation is represented by $\Im^{-1}$. Averaging the local estimates produced the final correlation.

III. Results

The validation of the technique follows. Figure 5 presents a comparison of the velocity fluctuation spectra measured using the Rayleigh technique and a hot-wire probe. Figure 5 shows that the shapes of velocity spectra are similar, whereas the absolute energy level in the spectrum measured by the Rayleigh technique is two and one-half times of that measured by the hot wire. The Rayleigh spectra float on a constant white noise floor, which is an expected consequence of electronic shot noise. Electronic shot noise creates the unavoidable, fundamental uncertainty in all optical intensity measurements. The photoelectron count in every time bin is contaminated by random fluctuations that follow a Poisson distribution. Spectra calculated from the time series of photoelectron counts obtained from still air, where there are no density or velocity fluctuations, show a white noise floor. The broadband, frequency-independent flat spectrum is a property of electronic shot noise. The propagation of electronic shot noise in the velocity spectrum

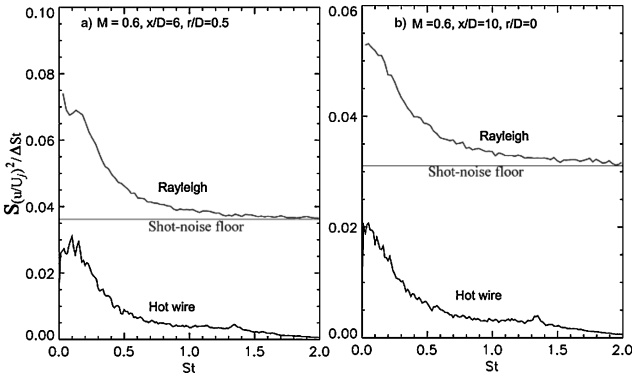

Fig. 5 Comparison of power spectral density of axial velocity fluctuations measured by Rayleigh technique and hot-wire probe at indicated locations of Mach 0.6 plume.

is somewhat complicated by the ratio of photoelectron counts, $R = N_3/N_2$, needed to determine instantaneous velocity. Nevertheless, the aforementioned spectral property was used to extract the standard deviation of the velocity fluctuations from the spectra. The measured fluctuations spectra $S_{u'^2}$ are due to a sum of the contributions from the shot noise (with mean square value σ^2_{shot}) and the desired velocity fluctuations (mean square u'^2_{rms}). The total energy under the power spectrum can be expressed as[14]

$$\int S_{u'^2}\,\mathrm{d}f = u'^2_{\text{rms}} + \sigma^2_{\text{shot}} \tag{17}$$

The constant shot noise floor was estimated as the average of spectral density values at the highest end of the resolved frequency, 40–45 KHz (Nyquest limit),

$$S_{\text{shot}} = \frac{1}{5000}\int_{f=40000}^{45000} S_{u'^2}\,\mathrm{d}f$$

The energy from turbulent fluctuations is expected to be small over this frequency range. Figure 5 shows the estimated noise floor for each Rayleigh spectrum. Because

$$\sigma^2_{\text{shot}} = \int S_{\text{shot}}\,\mathrm{d}f \tag{18}$$

the standard deviation of velocity fluctuations is

$$u'_{\text{rms}} = \sqrt{\int (S_{u'^2} - S_{\text{shot}})\,\mathrm{d}f} \tag{19}$$

The rms values measured by this shot noise subtraction process are found to be reasonable. For example, it is shown that $(u'_{\text{rms}}/U_j)_{\text{hot wire}} = 0.166$ and $(u'_{\text{rms}}/U_j)_{\text{Rayleigh corrected}} = 0.154$ and $(u'_{\text{rms}}/U_j)_{\text{hot wire}} = 0.14$ and $(u'_{\text{rms}}/U_j)_{\text{Rayleigh corrected}} = 0.132$. The subtraction method was used uniformly to estimate ρ'_{rms} and u'_{rms} from their respective spectrum.

Figures 6a, 6b, 7a, and 7b show typical velocity and density fluctuations spectra obtained from a region of very high turbulent fluctuations in Mach 1.4 and 0.95 plumes. A hot wire is unusable in these jets, and so only spectra measured by the Rayleigh technique are shown. Note that a narrowband notch filter centered at 430 Hz was applied to the velocity and density spectra. The unfiltered velocity fluctuations spectrum shows a large spike at this frequency. The spike was found to be independent of the jet speed and was attributed to a spurious oscillation in the incident laser frequency. As mentioned earlier, the laser head was placed directly underneath the jet, and the high noise level created by the plume is suspected to cause small vibrations in the laser cavity leading to the spike.[13] Nonetheless, the density and velocity fluctuations spectra are similar

Table 1 Standard deviations of density and velocity fluctuations, correlations between the two, and their impact on Favre averaging and SRA

x/D	r/D	Measured $u'_{\rm rms}/\bar{u}$	Measured $\rho'_{\rm rms}/\bar{\rho}$	$(\rho'_{\rm rms}/\bar{\rho})$ SRA $= (\gamma-1)M^2(u'_{\rm rms}/\bar{u})$	$\langle\rho';u'\rangle_{\tau=0}/\rho'_{\rm rms}\,u'_{\rm rms}$	$\langle\rho';u'u'\rangle_{\tau=0}/\rho'_{\rm rms}\,(u'u')_{\rm rms}$	$(\tilde{U}-\bar{U})/\bar{U}$	$\widetilde{(u''u'')}-\overline{u'u'})/\overline{u'u'}$
				$M_j = 1.8$				
10	0	0.067	0.067	0.082	0.29	−0.47	0.001	−0.037
12	0	0.094	0.09	0.09	0.59	−0.45	0.005	−0.047
14	0	0.125	0.087	0.097	0.65	−0.24	0.007	−0.027
16	0	0.15	0.085	0.086	0.62	−0.058	0.008	−0.008
3	0.45	0.041	0.04	0.054	0.26	−0.41	0.0004	−0.016
4	0.45	0.065	0.065	0.074	0.7	−0.7	0.003	−0.047
6	0.45	0.104	0.09	0.087	0.77	−0.38	0.007	−0.039
8	0.45	0.132	0.096	0.087	0.74	−0.23	0.009	−0.027
10	0.45	0.15	0.10	0.088	0.71	−0.11	0.01	−0.016
12	0.45	0.17	0.094	0.083	0.66	−0.074	0.011	−0.01
				$M_j = 1.4$				
10	0	0.087	0.073	0.051	0.55	−0.38	0.0036	−0.03
10	0.2	0.11	0.079	0.054	0.63	−0.18	0.005	−0.017
10	0.4	0.2	0.076	0.063	0.54	−0.3	0.008	−0.024
10	0.6	0.26	0.06	0.045	0.46	−0.08	0.007	−0.006
10	0.8	0.3	0.053	0.027	0.33	0.22	0.005	0.011
4	0.45	0.14	0.06	0.053	0.63	−0.13	0.005	−0.009
14	0	0.12	0.05	0.043	0.48	−0.07	0.003	−0.004
				$M_j = 0.95$				
10	0	0.1	0.04	0.028	0.45	−0.24	0.002	−0.01
14	0	0.12	0.03	0.024	0.28	0.04	0.001	0.001
4	0.45	0.14	0.041	0.027	0.47	−0.16	0.003	−0.007
6	0.45	0.19	0.04	0.032	0.43	−0.27	0.003	−0.011
10	0.45	0.23	0.034	0.03	0.4	−0.24	0.003	−0.008

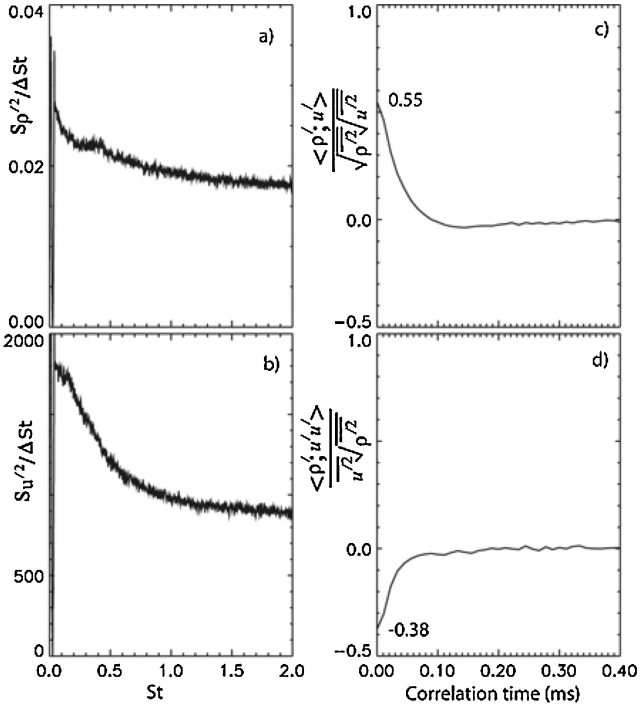

Fig. 6 Power spectral density of a) air density fluctuations and b) axial velocity fluctuations; correlation between c) density–velocity fluctuations and d) density–velocity squared fluctuations measured at $x/D = 10$ and $r/D = 0$ in Mach 1.4 jet.

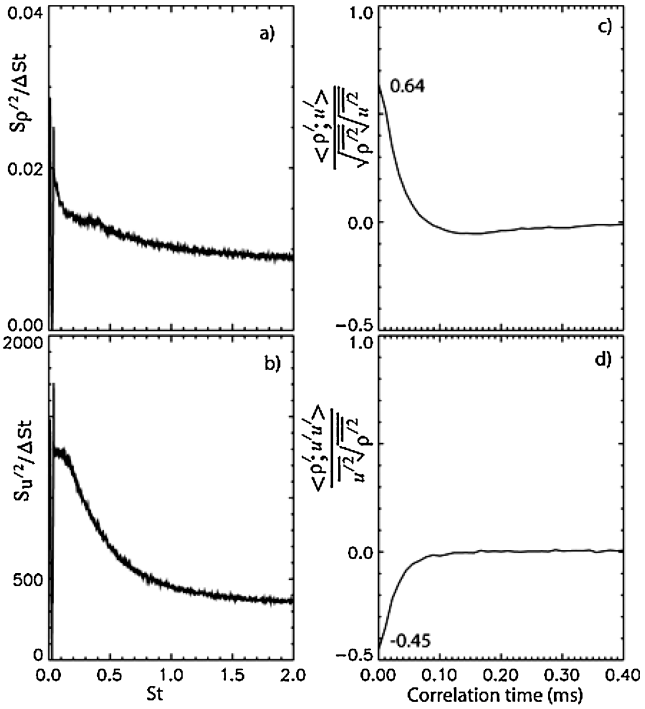

Fig. 7 Same as Fig. 6 except $M = 0.95$ jet, probe volume location $x/D = 10$, and centerline.

in shape. For the data shown in Figs. 6 and 7, the spectra show significant energy in the lowest frequency. The high-frequency rolloff is masked by the shot noise floor.

The cross-correlation calculations between density and velocity fluctuations, however, are mostly unaffected by shot noise. Because the shot noise contributions from different PMTs are uncorrelated, the cross-correlation process eliminates the influence of electronic shot noise and the absolute cross-correlation values are expected to have very small uncertainty. Figures 6c, 6d, 7c, and 7d show the nondimensionalized cross-correlation values measured in two different Mach number jets. Note that the correlations are expected to be symmetric in time; only the positive time delays are shown here. There are multiple interesting observations that can be made from Figs. 6c, 6d, 7c, and 7d. First, $\langle\rho';u'\rangle$ correlations are always fairly high and mostly positive. Second, $\langle\rho';u'u'\rangle$ correlations can be high or low depending on the Mach number and probe locations (Table 1). In the present unheated jets, positive values of the $\langle\rho';u'\rangle$ correlation are expected. The unheated jets cool to lower temperatures and higher densities than the ambient on expansion through the nozzle.

The high-velocity jet core has high density, whereas the quiescent ambient air has low density. Because the turbulent transport causes the high-velocity and high-density jet fluid to mix with the low-velocity and low-density entrained fluid, $\langle \rho'; u' \rangle$ correlations are positive. It is expected that if the same experiments were conducted in a heated jet, with a core density lower than the ambient density, negative correlations would have resulted. The negative values of the $\langle \rho'; u'u' \rangle$ correlations, on the other hand, cannot be explained by this argument. Following is a discussion of the uncertainty in the cross-correlation data.

The correlation values are normalized by individual standard deviations, which are the primary sources of uncertainty in the presented form. For example, correlations between velocity and density fluctuations are expressed as $\langle \rho'; u' \rangle / (\rho'_{\text{rms}} u'_{\text{rms}})$, which requires estimates of u'_{rms} and ρ'_{rms}. As mentioned, $\langle \rho'; u' \rangle$ correlations are relatively error free; however, the shot noise subtraction process described earlier has to be used to determine u'_{rms} and ρ'_{rms}. The subtraction process creates $\pm 10\%$ error in the standard deviation estimates. Hence, uncertainty levels of $\pm 20\%$ are expected on the quoted normalized correlation values. This large uncertainty supersedes all other sources, such as the contamination from temperature fluctuations, numerical convergence error, etc. It is also expected that the highest uncertainties are present in the lowest Mach number condition where the absolute values of density and velocity fluctuations are the lowest. The uncertainty level decreases with an increase in the jet Mach number.

The differences between Favre-averaged and Reynolds-averaged values are straightforward to calculate from the measured correlation data. For example, for the conditions shown in Fig. 6, the normalized differences between the Favre-averaged and the time-averaged axial velocity is calculated from Eqs. (5) and (12) using additional measured values of $\bar{\rho} = 1.45$ kg/m^3, $\bar{u} = 370$ m/s, $u'_{\text{rms}} = 32.3$ m/s, and $\rho'_{\text{rms}} = 0.11$ kg/m^3:

$$(\tilde{u} - \bar{u})/\bar{u} = \langle \rho'; u' \rangle_{\tau=0} / \bar{\rho}\bar{u} = 0.0036$$

Note that the large uncertainty in the normalized $\langle \rho'; u' \rangle / (\rho'_{\text{rms}} u'_{\text{rms}})$ does not affect the preceding estimate. Because the absolute values of the correlations are measured relatively accurately, the primary source of error is the uncertainty in $\bar{\rho}$ and $\bar{u}$ measurements. It is estimated that $(\tilde{u} - \bar{u})/\bar{u}$ is determinable within a maximum of $\pm 10\%$ uncertainty. The difference in the kinetic energy associated with the axial velocity fluctuations is calculated using Eqs. (10) and (12):

$$\frac{\widetilde{u''u''} - \overline{u'u'}}{\overline{u'u'}} = \frac{1}{\overline{u'^2}} \left[\frac{\langle \rho'; u'u' \rangle_{\tau=0}}{\bar{\rho}} - \left(\frac{\langle \rho'; u' \rangle_{\tau=0}}{\bar{\rho}} \right)^2 \right] = -0.03$$

The uncertainty in the preceding calculation is relatively higher due to the uncertainty in the $\overline{u'^2}$ estimates. The estimated level is $\pm 25\%$ of the quoted number.

A large number of data points were measured at many axial and radial locations in different Mach number plumes. Data analyzed from some selected conditions are shown in Table 1. A closer look at Table 1 confirms previous observations on $\langle \rho'; u' \rangle$ and $\langle \rho'; u'u' \rangle$ correlations. Additionally, it confirms that the Favre-averaged velocity is very slightly (from a fraction of a percent to 1%) higher than the Reynolds-averaged counterpart. Favre-averaging also produces a lower level (from a fraction of a percent to 4%) of kinetic energy compared to the Reynolds averaging. Notably, $\langle \rho'; u'u' \rangle$ correlations have a stronger impact than $\langle \rho'; u' \rangle$ correlations on the differences in the kinetic energy; a larger value of the former reflects as a larger difference between the two averaging process.

Table 1 also provides a comparison of the measured air density fluctuations $\rho'_{\text{rms}}/\bar{\rho}$ with that estimated from velocity fluctuations $u'_{\text{rms}}/\bar{u}$ using Morkovin's SRA [Eq. (3)]. On average, SRA is found to underpredict density fluctuations; however, a closer look shows a Mach number dependence. For the highest $M = 1.8$ jet, SRA-predicted density fluctuations are in reasonable agreement with the measured data. For the lower $M = 1.4$ and 0.95 jets, the predicted fluctuations are lower than the measured data. The differences are particularly large in regions with vigorous turbulent fluctuations such as the end of the potential core and the middle of the lip shear layer.

IV. Summary

A molecular Rayleigh scattering based optical measurement technique was used to simultaneously measure air density and the axial component of velocity at a sampling rate of 90,000/s. The density variation was measured by monitoring the variation of the total scattered light intensity. The velocity variation was measured by spectrally resolving the scattered light using a Fabry–Perot interferometer and monitoring the time-dependent Doppler shift from the incident laser frequency. A small probe volume length of 1.03 mm and diameter 0.2 mm allowed point measurements from different regions of the flowfield. One convergent and two convergent–divergent nozzles were used to produce unheated plumes with Mach numbers 0.8, 0.95, 1.4, and 1.8. The standard deviations of the density fluctuations ρ'_{rms} and axial velocity fluctuations u'_{rms}, along with cross correlations, density–velocity $\langle \rho'; u' \rangle$ and density–velocity^2 squared $\langle \rho'; u'u' \rangle$, measured from different regions of the plumes, provided the following results:

1) Normalized $\overline{\rho'u'}$ correlations are significantly high (vary between 0.3 and 0.8) and are always positive. The positive correlation is expected in the unheated plume where the jet core has higher density than the ambient.

2) Normalized $\overline{\rho'u'u'}$ correlations are also high (mostly vary between -0.1 and -0.5) and are almost always negative.

3) The Favre-averaged axial velocity is very slightly (fraction of a percent to 1%) higher than the Reynolds-averaged counterpart.

4) The axial component of turbulent kinetic energy calculated via Favre-averaging, $0.5\,\widetilde{u''u''}$, is lower by a fraction of a percent to 4% from the same quantity calculated via Reynolds averaging, $0.5\,\overline{u'u'}$.

5) The estimation of turbulent density fluctuations from the axial velocity fluctuations, using Morkovin's SRA, is found to provide lower values compared to the measured data at the lower Mach number conditions. The estimates are found to improve at the highest jet Mach number of 1.8.

The present experiments were conducted in unheated jets where the stagnation temperature of the plume was the same as that of the ambient. It will be of interest to conduct similar experiments in heated jets where the effect of total temperature fluctuations on the foregoing parameters can be established.

Acknowledgments

This work was funded by NASA's Quiet Aircraft Technology program. We acquired these experimental data as part of a jet noise source identification study. The first author acknowledges encouragement from James Bridges of NASA John H. Glenn Research Center at Lewis Field in performing this part of the data analysis.

References

[1]Favre, A., "Équations Fondamentales des Fluids à Masse Volumique Variable en Écoulements Turbulents," *La Turbulence en Mécanique des Fluides*, edited by A. Favre, L. S. G. Kovasznay, R. Dumas, J. Gaviglio, and M. Coantic, Centre National de la Recherche Scientifique, 1976, pp. 74–78.

[2]Smits, A. J., and Dussauge, J. P., *Turbulent Shear Layers in Supersonic Flow*, Springer-Verlag/AIP Imprint, Woodbury, NY, 1996.

[3]Bowersox, R. D. W., "Combined Laser Doppler Velocimetry and Cross-Wire Anemometry Analysis for Supersonic Turbulent Flow," *AIAA Journal*, Vol. 34, No. 11, 1996, pp. 2269–2275.

[4]Morkovin, M. V., "Effects of Compressibility on Turbulent Flow," *Mechanics of Turbulence*, edited by A. J. Favre, Gordon and Breach, New York, 1964, pp. 367–380.

[5]White, F. M., *Viscous Fluid Flow*, McGraw–Hill, New York, 1973.

[6]Bradshaw, P., "Compressible Turbulent Shear Layers," *Annual Review of Fluid Mechanics*, Vol. 9, 1977, pp. 33–52.

[7]Gaviglio, G., "Reynolds Analogies and Experimental Study of Heat Transfer in the Supersonic Boundary Layer," *Journal of Heat and Mass Transfer*, Vol. 30, No. 5, 1987, pp. 911–926.

[8]Barre, S., Quine, C., and Dussauge, J. P., "Compressibility Effects on the Structure of Supersonic Mixing Layers: Experimental Results," *Journal of Fluid Mechanics*, Vol. 259, 1994, pp. 47–78.

[9]Seasholtz, R. G., Panda, J., and Elam, K. A., "Rayleigh Scattering Diagnostic for Measurement of Velocity and Density Fluctuation Spectra," AIAA Paper 2002-0827, 2002.

[10]Seasholtz, R. G., Panda, J., and Elam, K. A., "Rayleigh Scattering Diagnostics for Dynamic Measurement of Velocity Fluctuations in High Speed Jets," AIAA Paper 2001-0847, 2001.

[11]Panda, J., Seasholtz, R. G., Elam, K. A., and Mielke, A. F., "Time-Averaged Velocity, Temperature and Density Surveys of Supersonic Free Jets," American Society of Mechanical Engineers, Paper HT-FED2004-56856, 2004.

[12]Panda, J., and Seasholtz, R. G., "Experimental Investigation of Density Fluctuations in High-Speed Jets and Correlation with Generated Noise," *Journal of Fluid Mechanics*, Vol. 450, 2002, pp. 97–130.

[13]Panda, J., Seasholtz, R. G., and Elam, K. A., "Further Progress in Noise Source Identification in High Speed Jets via Causality Principle," *Journal of Fluid Mechanics*, Vol. 537, 2005, pp. 349–385.

[14]Saleh, B. E. A., and Teich, M. C., *Fundamentals of Photonics*, Wiley, New York, 1991.

N. Chokani
Associate Editor